Article

ANN-Based Assessment of Soft Surface Soil Layers' Impact on Fault Rupture Propagation and Kinematic Distress of Gas Pipelines

Nikolaos Makrakis [1], Prodromos N. Psarropoulos [2] and Yiannis Tsompanakis [1,*]

[1] School of Chemical and Environmental Engineering, Technical University of Crete, 73100 Chania, Greece
[2] School of Rural, Surveying and Geoinformatics Engineering, National Technical University of Athens, 15780 Athens, Greece
* Correspondence: jt@science.tuc.gr; Tel.: +30-28210-37634

Abstract: Large-scale lifelines in seismic-prone regions very frequently cross areas that are characterized by active tectonic faulting, as complete avoidance might be techno-economically unfeasible. The resulting Permanent Ground Displacements (PGDs) constitute a major threat to such critical infrastructure. The current study numerically investigates the crucial impact of soil deposits, which usually cover the ruptured bedrock, on the ground displacement profile and the kinematic distress of natural gas pipelines. For this purpose, a decoupled numerical methodology, based on Finite Element Method (FEM), is adopted and a detailed parametric investigation is performed for various fault and soil properties. Moreover, the advanced capabilities of Artificial Neural Networks (ANNs) are utilized, aiming to facilitate the fast and reliable assessment of soil response and pipeline strains due to seismic faulting, replacing time-consuming FEM computations. An extensive sensitivity analysis is performed to select the optimal architecture and training algorithm of the employed ANNs for both the geotechnical and structural parts of the decoupled approach, with suitable input and target values related to bedrock offset, fault and soil properties, surface PGDs, and pipeline strains. The proposed ANN-based approach can be efficiently applied by practice engineers in seismic design and route optimization of natural gas pipelines.

Keywords: seismic faulting; fault rupture propagation; permanent ground displacements; kinematic distress; gas pipelines; finite element method; artificial neural networks

1. Introduction

The constantly increasing demands on energy supplies and telecommunication has led to the continuous development (i.e., design, construction, and operation) of large-scale lifelines, such as high-pressure gas or—in the near future—hydrogen pipelines, as well as telecommunication and energy (i.e., power transmission) cables. Lifelines constitute critical and expensive facilities that extend for hundreds to thousands of kilometers, onshore and/or offshore. Consequently, lifelines often cross areas that are seismically active, imposing a serious threat to their structural integrity and safe function. It is worth noting that many severe failures of pipelines have been reported due to earthquake events [1].

Large-scale lifelines are vulnerable to soil deformations due to earthquake-related geohazards, such as tectonic faulting, soil liquefaction, lateral spreading, and slope instabilities, causing so-called Permanent Ground Displacements (PGDs). Since the complete avoidance of seismic-prone areas that are susceptible to earthquake-triggered geohazards is unavoidable and/or unfeasible due to environmental, technical, and financial reasons, the accurate and reliable assessment of PGDs and the consequent distress of lifelines is a topic of paramount importance.

Regarding the structural performance of buried pipelines subjected to the geohazard of seismic fault rupture, extensive analytical, numerical and experimental studies

have been presented over the last decades. More specifically, Newmark and Hall [2], Kennedy et al. [3], and Wang and Yeh [4] pioneered the analytical investigation of the fault–pipeline intersection problem. Numerical methodologies have been gradually developed, typically based on the Finite Element Method (FEM), utilizing either coupled [5–8] or decoupled [9–12] approaches, in which the pipeline and the surrounding soil (or rock) are numerically simulated in unified or separate FE models (i.e., one for the wider soil/rock stratum and one for the pipeline), respectively. The pipe–soil interaction is simulated in coupled FEM utilizing appropriate contact elements, whereas in decoupled FEM via bi-linear soil springs or interface elements that transfer the PGDs from the soil FE model and impose them to the pipeline. More advanced numerical methodologies have also been developed, taking into account the surrounding soil irregularities, the non-linearities of pipe–soil interaction, as well as the crucial role of pipeline service loads [13–15]. On the other hand, full-scale tests [16,17] and—less demanding and more cost effective—small-scale physical experiments [6,18], as well as centrifuge tests [19,20] have been performed to evaluate the critical role of several factors (e.g., fault, pipeline, and soil characteristics) on the structural performance of a pipeline subjected to tectonic faulting.

The fact that widely-applicable international guidelines and norms, such as ASCE guidelines [21], American Lifelines Alliance [22], and Eurocode 8 [23], have been developed for the design of pipelines facing the earthquake-induced geohazard of fault rupture highlights the significance of the fault–pipe intersection problem. However, the problem of fault–pipe intersection considering the presence of soft soil layer(s) that usually cover the rigid bedrock has not been addressed in the majority of the aforementioned studies, as it is usually considered that the pipeline is—rather unrealistically—laid directly on bedrock (Figure 1). Nonetheless, the overlying soil cover, with thickness varying from tens to hundreds of meters depending on local site conditions, may have a critical impact on aboveground or buried gas pipelines. In general, seismic fault rupture, which occurs in the stiff Earth's crust, is directly related to abrupt bedrock displacements that very often propagate through overlying soil deposit(s) and may even reach the ground surface, thus posing a serious threat to large-scale lifelines (Figure 2). Hence, it becomes evident that the problem of fault–pipe intersection may be considerably affected not only by fault rupture, but also by the related phenomena of fault rupture propagation and fault outcropping.
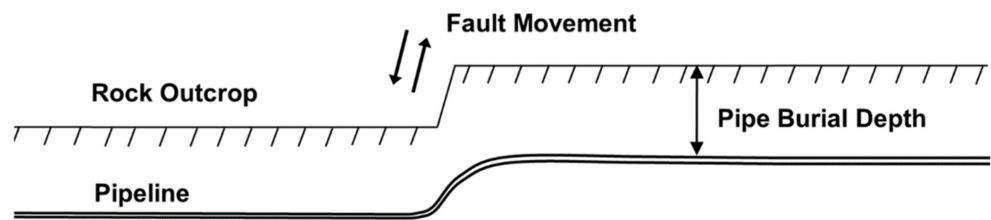
Figure 1. Pipeline laid directly on bedrock, subjected to fault rupture.
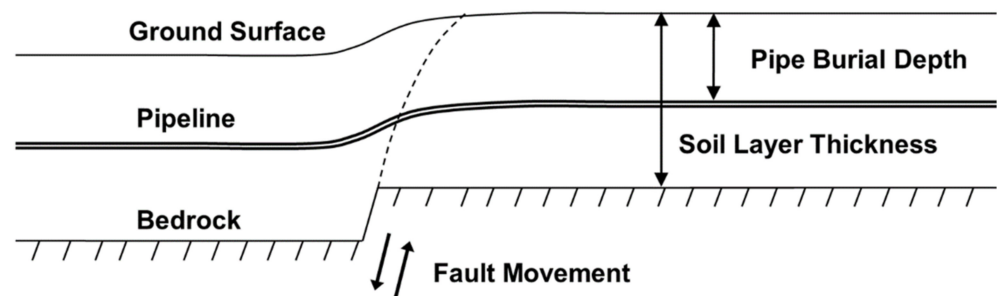
Figure 2. Pipeline buried inside a soil layer, subjected to fault rupture.

Nonetheless, the impact of overlying soil strata on buried pipelines that cross active seismic faults has not attracted intense research interest up to now. Tsatsis et al. [6] have numerically and experimentally investigated: (i) the phenomenon of fault rupture prop-

agation considering a cohesionless soil cover, and (ii) the associated distress of a buried pipeline subjected to dip-slip faulting. Similarly, Fadaee et al. [7] conducted a detailed numerical investigation regarding the impact of pipe thickness and burial depth, as well as overlying soil layer thickness, on the structural performance of buried steel pipelines subjected to reverse faulting. In related studies of authors' group (Makrakis et al. [24,25]), a series of decoupled numerical analyses have been performed, taking into account the presence of soft soil layers that cover the rigid bedrock. The ground surface inclination, which is directly related to the developed PGDs, has been associated with fault dislocation level [24]. A similar methodology has been developed to realistically capture the kinematic distress of buried steel pipelines, in terms of strains, due to fault rupture propagation and outcropping at ground surface [25]. Based on a regression analysis, suitable simple relationships have been derived to correlate both the levels of ground surface inclination and pipe distress with the earthquake magnitude, in terms of bedrock movement.

The literature review has revealed that the phenomena of fault rupture and fault rupture propagation, as well as the problem of fault–pipe intersection, have been investigated by means of conventional numerical and experimental methodologies. Both are undoubtedly subject to cost and time constraints, since a large number of computationally demanding numerical analyses and/or space- and cost-demanding experimental programs are required for a realistic and accurate examination of the problem at hand. Hence, an efficient way to overcome potential difficulties and constraints is the application of Soft Computing (SC) and Machine Learning (ML) techniques, as proposed in the current study.

Over the recent years, SC and ML techniques are becoming more widely applicable due to the continuous developments of related methods and the increase of available computational resources. Accordingly, SC and ML have emerged as a promising and attractive alternative to conventional and time-consuming methodologies. In particular, such techniques can easily capture the complex or even unknown non-linear relationship between input and output variables of phenomena and problems characterized by multidisciplinary nature and uncertainties [26]. The inherent and distinct advantages of SC and ML techniques, such as the increasing predictive performance and flexible model interpretability, have been reported by several studies in a wide range of applications [27]. SC techniques have been utilized in infrastructure engineering applications [28,29], as well as earthquake engineering problems [30,31]. On the other hand, ML has also been widely used in structural engineering [32], soil mechanics [33], earthquake engineering [34,35], as well as in geohazard detection, mapping, and risk assessment [36–40].

Artificial Neural Networks (ANNs), introduced by McCulloch and Pitts in 1943 [41], constitute one of the most commonly used methods of ML. In general, ANNs can be considered as a powerful tool capable of correlating specific input and output values via linear or non-linear relationships [42]. The purpose of ANNs is to imitate the human brain functioning via proper computational elements, known as neurons or nodes, which are connected with transfer functions that define the links among them [43]. Due to their unique characteristics, ANNs have been applied in many complex problems in various fields, such as pattern recognition, decision-making, regression (function approximation/fitting), and optimization. ANNs have been widely used in a variety of simple and more demanding applications of structural engineering, including probabilistic reliability analyses and optimization problems [44–46], engineering seismology [47], earthquake engineering [48–50] and structural earthquake engineering [51,52], as well as geotechnical and geotechnical earthquake engineering [53–58]. In general, ANNs have been successfully used in various engineering problems because they can efficiently and reliably replace the computationally demanding FEM calculations. Such surrogate metamodels can drastically reduce the computational cost and provide fast predictions of the non-linear relationships between the input and target values [59–63].

Research effort has been concentrated up to now on the assessment (i.e., susceptibility, risk, and hazard analysis) of specific earthquake-related geohazards, such as slope stability and soil liquefaction, as well as on the seismic response of buildings, embankments, and

bridges. To the best of authors' knowledge, ANNs have not been used for the simulation of the geohazard of seismic fault rupture and the resulting pipeline kinematic distress due to fault–pipe intersection. Hence, the main novelty of this work is the proposed ANN-based metamodels, which aim to facilitate the reliable and accurate assessment of PGDs and the resulting distress of buried steel pipelines, due to the fault rupture, fault rupture propagation, and fault outcropping. For this purpose, dip-slip fault motion corresponding to different loading conditions, as well as sandy overlying soil layers of varying thickness and mechanical properties, have been considered. The extensive dataset developed from the parametric investigation of authors' relevant studies [24,25] is herein enriched with additional FEM analyses. Subsequently, it is utilized to feed two separate ANNs, which are created following the decoupled approach, to deal with the problem at hand. The industry and engineering practice can significantly benefit from the proposed ANN-based approach that can be efficiently utilized in the seismic design and route optimization of natural gas pipelines, replacing time-consuming FEM analyses.

The rest of the paper is organized as follows: Section 2 contains a detailed description of the utilized materials and methodologies. Firstly, the empirical correlation of earthquake magnitude with bedrock displacement is sufficiently explained. Then, the FE mesh discretization, the boundary, and loading conditions of the proposed FE models, as well as the structure of the employed ANNs, are described. Section 3 initially presents the results of the detailed numerical investigation and, subsequently, describes the datasets used for training ANNs. Furthermore, the results derived from the application of the developed ANNs are presented by means of training evaluation metrics and duration. Section 4 discusses the results that have been obtained from the numerical modeling of fault rupture propagation and fault–pipe intersection, and compares them with the related predictions of the developed ANNs. Finally, Section 5 presents the main findings of the study, as well as the limitations and the potential extensions of the proposed methodology.

2. Materials and Methods

Regarding fault rapture, the current study utilizes a well-established expression that correlates earthquake magnitude with bedrock displacement. More specifically, Wells and Coppersmith [64] developed a set of empirical relationships regarding the average and maximum bedrock displacement due to fault rupture (*AD* and *MD*, respectively), and the seismic intensity by means of the moment earthquake magnitude, M, as follows:

$$\log(AD) = a + b \cdot M \tag{1}$$

where the regression coefficients a and b are set equal to -4.80 and 0.69, with 0.36 standard deviation, and 0.57 and 0.08 standard errors, respectively. It is worth noting that Equation (1) is valid for *M* values ranging between 5.6 and 8.1 and *AD* from 0.05 to 8.0 m. In the current investigation, quite high magnitude values (*M* = 6.5, 7.0, 7.5) have been used and the resulting *AD* values of the bedrock offset are used in the numerical simulations.

2.1. Numerical Simulations

In general, during a seismic event, the rupture of an earthquake fault generates two types of ground movement: permanent quasi-static offsets on the seismic fault itself, and transient dynamic oscillations away from the fault, the so-called Permanent Ground Displacements (PGDs) and Transient Ground Displacements (TGDs), respectively. The latter are critical for structures with considerable mass (e.g., buildings and bridges) due to the developed inertial forces, while the former may play a detrimental role in the structural performance of lifelines (e.g., pipelines and cables) which have rather small mass. Hence, considering that the seismic kinematic distress is the main concern for pipelines, the problem of fault–pipe intersection can be realistically simulated by means of quasi-static loading.

The phenomenon of fault rupture, along with the related phenomena of fault rupture propagation and fault outcropping, as well as the problem of fault–pipe intersection, have

been realistically simulated utilizing ABAQUS finite element software [65]. A decoupled FE modeling approach has been employed, where the soil response due to fault rupture has been quasi-statically simulated utilizing the Dynamic-Explicit module of ABAQUS. On the other hand, the pipe–soil interaction has been modeled utilizing the Static-Standard module of ABAQUS. These analysis modules have been selected to ensure numerical stability of both models. It should be mentioned that the critical inertia effects play a key role in dynamic analyses, and thus, to achieve reliable pseudo-static results, proper loading rates have been selected by taking into account that the maximum kinetic energy of the FE model should range between 5–10% of the total energy, as proposed by Ni et al. [66].

Figure 3 illustrates the proposed numerical model for the soil response due to fault rupture. The suggestions of several researchers regarding FE model development and analysis have been adopted herein [67–70]. In particular, a uniform soil stratum of thickness H is assumed to cover the rigid bedrock and has been simulated in 2D plane-strain conditions with four-node quadrilateral elements (type CPE4). Having performed an extensive sensitivity analysis related to the minimization of undesired boundary effects, the width of the FE model, B, has been selected equal to 4H or 8H, depending on H value. Additionally, to achieve optimal numerical performance, a finer FE mesh discretization has been chosen for the failure plane (i.e., at the middle of the FE model). Indicatively, Figure 3 depicts the FE mesh discretization of a 50 m-thick soil layer.
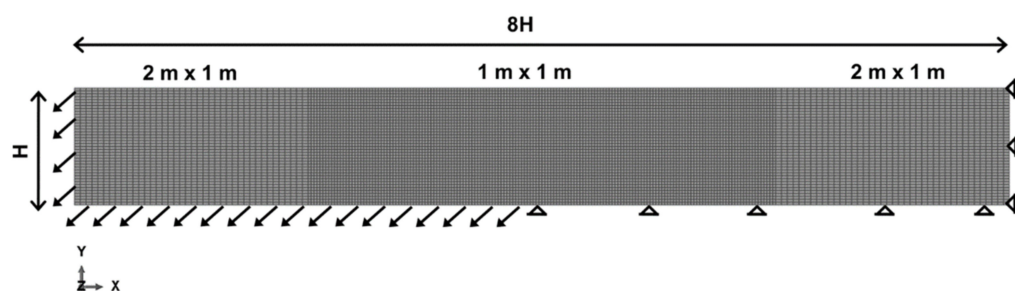
Figure 3. FE mesh, loading and boundary conditions for a 50 m-thick soil layer.

The numerical analyses have been performed via two loading steps: a geostatic step, in which gravity loads are applied; subsequently, a differential displacement at an angle α (i.e., fault dip angle) parallel to the fault plane is imposed. Figure 3 displays the loading and boundary conditions of the soil FE model. The hanging wall of the fault is represented by moving the left side (vertical and bottom nodes) of the FE model parallel to the fault plane, enforcing the specific level of fault offset, whereas the foot wall is simulated considering fixed right bottom nodes and imposing roller boundary conditions at the right vertical side of the FE model.

The two-node PIPE21 elements, known also as Timoshenko beam elements, have been selected to numerically represent a pipeline with meticulously constructed welded connections, which can be considered as continuous (i.e., not segmented). Pipe–soil interaction has been simulated by means of PSI24 interaction elements along the axial and vertical directions. PSI24 usually lead to more accurate and realistic results compared to the conventional soil springs, consisting of four nodes. The two nodes are attached to the pipe, while the other two represent the soil, thus facilitating the assessment of soil resistance. It is noted that the pipeline can be modeled more accurately using shell elements and the surrounding soil (or rock) stratum can be modeled with 3-D solid elements, while their interaction can be simulated utilizing appropriate contact elements. Nonetheless, such simulations require much higher computational cost; thus, they are not suitable for extensive parametric investigations. Taking also into account the successful validation of both numerical models in authors' previous works with available experimental and numerical results [11], they can be considered as adequate for the purposes of the current study.

Figure 4 provides a description of the employed numerical modeling of the pipeline and pipe–soil interaction. In order to achieve optimal modeling and ensure numerical

convergence, the pipe as well as the PSI elements have the same size as the soil elements of the first FE model. Furthermore, a pipeline of typically infinite length is simulated to ensure the minimization of undesirable effects of boundary conditions at the edges of the FE model. The end of the pipeline, as well as the far-field PSI nodes towards the foot wall soil block, are fixed, whereas the opposite end and the associated far-field PSI nodes (i.e., towards the hanging wall) follow the fault movement. The PGDs along the axial and vertical directions, which have been derived from the geotechnical FE model, are imposed on the pipeline through the PSI elements, within a critical length equal to soil model width (i.e., 4H or 8H).
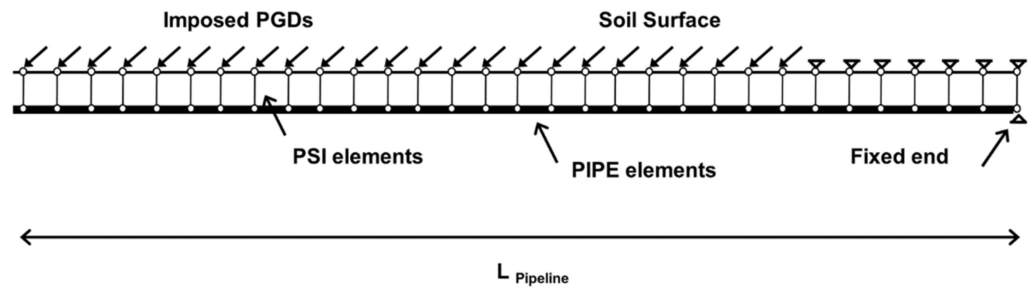
Figure 4. Numerical modeling of a buried pipeline and pipe–soil interaction.

It is important to mention that soil non-linearities have to be suitably simulated due to large levels of ground deformations for high seismic magnitude levels. Hence, to realistically capture the non-linear soil response due to fault rupture, the elastoplastic Mohr-Coulomb constitutive model with isotropic strain softening is adopted [68]. More specifically, an elastic pre-yield soil behavior is assumed, whereas the Mohr–Coulomb failure criterion is utilized to capture the post-peak soil response. Hence, in the employed isotropic strain softening, the mobilized friction and dilation angles are linearly decreased as the octahedral plastic shear strain, γ^p_{oct}, increases:

$$\varphi = \begin{cases} \varphi_p - \frac{\varphi_p - \varphi_{res}}{\gamma^p_f}\gamma^p_{oct} & \text{for } 0 \leq \gamma^p_{oct} < \gamma^p_f \\ \varphi_{res} & \text{for } \gamma^p_{oct} \geq \gamma^p_f \end{cases} \tag{2}$$

$$\psi = \begin{cases} \psi_p(1 - \frac{\gamma^p_{oct}}{\gamma^p_f}) & \text{for } 0 \leq \gamma^p_{oct} < \gamma^p_f \\ \psi_{res} & \text{for } \gamma^p_{oct} \geq \gamma^p_f \end{cases} \tag{3}$$

where φ and ψ denote the friction and dilation angles, respectively. φ_p and φ_{res} correspond to the ultimate mobilized (peak) and residual friction angles, while ψ_p and ψ_{res} are the corresponding dilation angles, and γ^p_f represents the failure plastic octahedral shear strain at the end of strain softening. The aforementioned soil constitutive model has been applied in ABAQUS via a subroutine that has been developed by authors' group [11]. Additionally, the critical impact of scale effects on the failure plastic octahedral shear strain at the end of strain softening has been successfully taken into account by setting the d_{FE}/d_B ratio equal to the ratio of the real shear strain over the FE-computed shear strain [68], where d_{FE} is the FE mesh size and d_B denotes the shear band thickness. Lastly, it is important to mention that the accuracy of both numerical models has been verified utilizing the experimental results of Anastasopoulos et al. [68] for the geotechnical model and Tsatsis et al. [6] for the soil–pipe interaction model. More information on these validations can be found in Chatzidakis et al. [11].

2.2. Artifical Neural Networks

A feedforward network architecture, also known as multi-layer perceptron (MLP) network [71], has been selected for the purposes of the current study. In general, Feedforward Neural Networks (FFNNs), which consist of the input, the hidden (or intermediate), and

the output layers, are the most common ANN type. Their main characteristic is that they update the information from the input variables to the output layer only in one direction, without back connections (i.e., recurrent links between the layers) [72]. Although FFNNs may include several hidden layers (the so-called "deep" networks), studies investigating the role of ANNs on the earthquake-induced geohazards (e.g., [58]) have demonstrated that the number of hidden layers has a marginal impact on the results. Hence, "shallow" (having one or two hidden layers) feedforward NNs have been utilized herein, taking advantage of the capabilities of the NN toolbox in MATLAB computational platform [73].

Due to their simpler structure compared to deep networks, shallow FFNNs consisting of a single (Figure 5) or two (Figure 6) hidden layer(s) are characterized by faster training capabilities, less effort for parameter fine-tuning, and easier understanding of their performance. Consequently, shallow NNs are suitable for relatively small datasets, such as the ones used in the present study. Each layer contains a number of units, also known as neurons, while the information is transmitted from one layer to the other via suitable transfer functions [43]. Initially, the independent input variables (i.e., known data) are fed into the input layer. The neurons of the input layer, which are directly related to the number of input variables, receive the information and they transmit it to the hidden layer(s). The latter play a crucial role, since they correlate the neurons of the input layer in order to define the relationship among the input data. The information reaches the output layer, which is connected with the hidden layer(s), and the results of the network are ultimately generated.
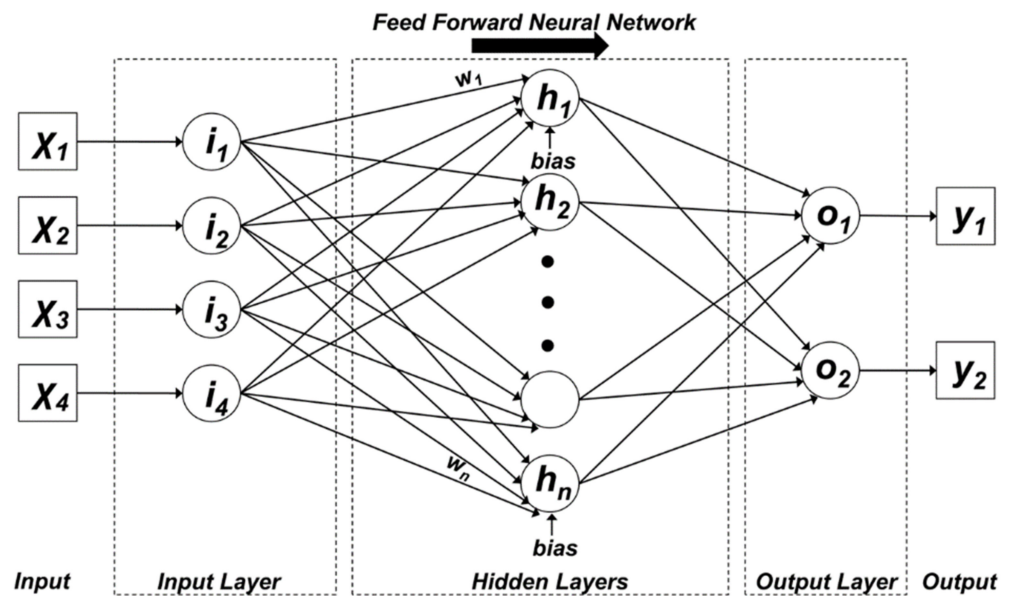
Figure 5. Feed Forward Neural Network consisting of a single hidden layer.

It is worth noting that all neurons between the neighboring layers are fully connected to each other by weights and biases. In particular, the neurons of each layer multiply the input values by weights and add the bias values. The sum of the weights and biases, *n*, is then delivered to next layer through the transfer function, *f(n)*. Sigmoid neurons have been selected for the hidden layer(s), in which a standard log-sigmoid transfer function is used:

$$f(n) = \frac{1}{1 + e^{-n}} \tag{4}$$

whereas a linear transfer function has been utilized for the output layer. These are the most commonly used activation functions for NN-based earthquake engineering applications due to their simple form and satisfactory performance (e.g., [34,47]).
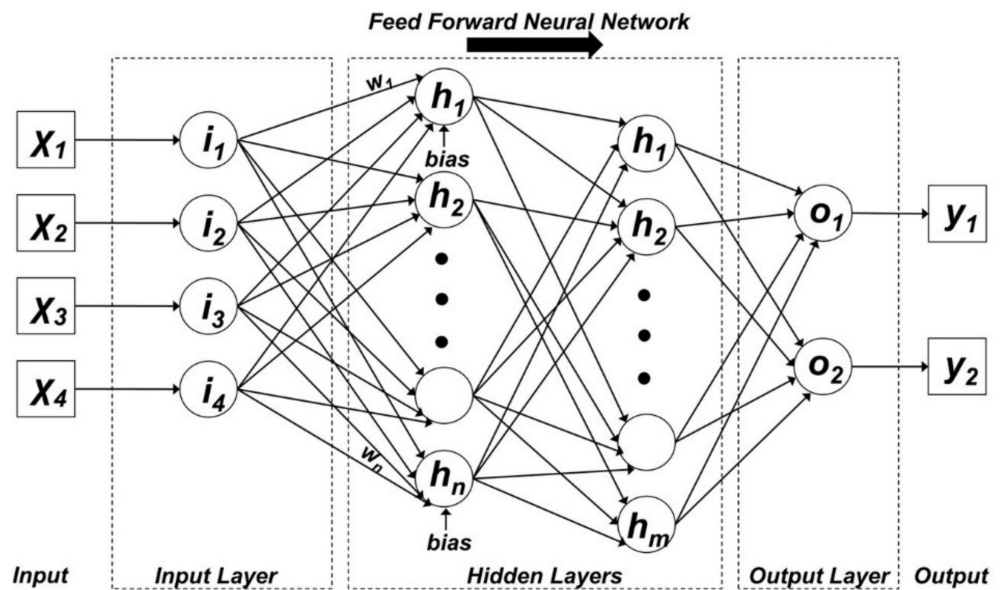
Figure 6. Feed Forward Neural Network consisting of two hidden layers.

Another important aspect when configuring ANN architecture is to define the number of neurons of the hidden layer(s). If a small number of hidden neurons is selected, a poor learning model might be created, incapable of obtaining the relationships between the data, causing the so-called "underfitting" [74]. Conversely, increasing the number of hidden neurons is not always the optimal solution. Although over-increasing hidden neurons can lead to networks capable of efficiently solving more complex problems, the generated networks may have the tendency to memorize the training data, thus causing "overfitting". As a consequence, the training information loss will be significantly reduced, but the generated NNs will fail to perform well when they are fed with new data due to the variance of model parameters [75]. Hence, it becomes evident that selecting the proper number of hidden neurons constitutes a challenging issue when constructing a NN, since there are only heuristic rules that can be adopted, depending on the special characteristics of the examined problem. As a consequence, an extensive sensitivity analysis has been performed varying the number of hidden layer(s) neurons, following the suggestions reported in several studies [58,62,63,76].

In general, data division plays a key role in the generated network in order to avoid underfitting or overfitting. The input dataset is divided into three subsets: training, where the weights and biases of the network are computed, testing, and validation. In most cases 70–80% of the dataset is used for training the network, whereas the remaining 20–30% is used to test its performance [58]. Herein, considering that the datasets are quite small, they have been divided so that 80% is used for training, while the remaining 20% is equally assigned to the validation and test subsets, respectively. Since the initial synaptic weights are randomly set, the training process has been repeated a reasonable number of times. More specifically, 30 independent (i.e., without keeping track of the other runs) trainings sessions have been performed for each ANN architecture. In each re-training, the available data are randomly distributed to form the 80%, 10%, 10% training, validation, and test subsets. It is noted that training improvement techniques can been applied in future extensions, e.g., due to their small size of the datasets, the validation set can also be used during the training process as part of the training set, aiming to improve the generalization capabilities of the metamodels [77].

Although many different training algorithms have been gradually developed, the capabilities of shallow FFNNs in yielding better results are based on the backpropagation process when applied to: (i) complex and non-linear problems, and (ii) incomplete and ambiguous input variables [78]. More specifically, during the training session of a network using back propagation algorithm, a comparison between the results of the NN and

the target values is performed, and the resulting prediction errors are then layer-to-layer propagated backwards to apply adjustments to the synaptic weights. Herein, the well-known Levenberg–Marquardt (LM) backpropagation algorithm has been utilized, as it is characterized by small training duration. It is noted that the application of LM might be impractical for extremely large datasets [79]. Taking into account that NNs may lead to poor predictions when adding new data, since they are prone to "overfitting", several techniques have been developed, such as regularization and "early stopping" [80]. The regularization methodology, where the different features of the network are penalized by multiplication with a factor, λ, has generally led to functional and less complex networks. The current study has additionally adopted one of the most popular regularization methodologies, known as Bayesian Regularization (BR). Although both LM and BR methodologies are not so memory-efficient, since they are based on the Jacobian calculations, they are recommended for most problems [80]. Particularly, for small and noisy datasets, BR is expected to lead to a better solution, while it also increases the associated computational cost.

The role of backpropagation training process of each network is twofold: (i) to tune the hyperparameters (i.e., the parts of the network that play a significant role in the final accuracy and prediction capabilities of the NN), and (ii) to derive the model weights and biases. Certainly, establishing the optimal structure and the optimal training process of a network are very challenging topics, which may lead to unreliable (under- or over -fitted) models, due to some deficiencies that characterize ANNs. Firstly, each network relies on different "initial" conditions, i.e., different values on the initial weights and biases, while each network provides different data on training, validation, and test sets. Thus, different solutions may be obtained for the same problem. Therefore, for small and ambiguous datasets, an adequate number of retraining sessions—as performed in the current study—can be an efficient means to finetune network parameters, as well as to overcome the problem of weight and biases initial conditions. Additionally, ANNs can be characterized as "black-box" models, since there is not a clear understanding of their operation, and subsequently, the final output cannot be easily explained and justified. Thus, the trial-and-error approach constitutes a reasonable strategy to understand the results and assess the performance of the generated NNs [62,76].

Lastly, several metrics have been utilized to assess the performance of the developed NNs, such as time and space, as well as loss functions (i.e., performance functions). The latter usually vary according to the learning task and the nature of the problem [81]. Mean Squared Error (MSE), square Root of the Mean Squared Error (RMSE), as well as Mean Absolute Error (MAE) constitute typical performance functions for the developed FFNNs [82] and have also been used in this investigation. In particular, the overall performance of the generated NNs has been evaluated by means of the RMSE and the coefficient of determination, R^2, of the results. The lower the value of RMSE and the higher the value of R^2, the better the performance of the NN. More specifically, RMSE quantitatively indicates how the predicted values (output) differ from the actual values (targets), whereas R^2 ranges between 0 and 1, and it is a reliable indicator of the linear relationship between the output and target values [82]. Typically, RMSE and R^2 are mathematically expressed as follows:

$$R^2 = 1 - \frac{\sum\limits_{i=1}^{n}(y_i - y\prime_i)^2}{\sum\limits_{i=1}^{n}(y_i - \overline{y})^2} \tag{5}$$

$$\text{RMSE} = \sqrt{\frac{\sum\limits_{i=1}^{n}(y_i - y\prime_i)^2}{n}} \tag{6}$$

where y and $y\prime$ denote the actual and predicted values, respectively; $\overline{y}$ is the average of the actual values; and n represents the total number of data samples.

3. Results

A series of FE analyses has been performed considering a dip-slip fault (i.e., normal fault). Three levels of bedrock offset have been simulated, corresponding to earthquake magnitude equal to M = 6.5, 7.0, and 7.5, while the resulting bedrock dislocation is computed via Equation (1). Moreover, three dip angles, α, equal to 30°, 45°, and 60°, have been considered. An overlying soil layer with thickness, H, ranging between 20 m and 100 m, has been assumed to cover the rigid bedrock. The specific M values cover adequately the main purposes of the present study, e.g., for lower M, the pipe will not exhibit high strain levels. Moreover, as it will be shown in the sequence, the ANNs provide quite satisfactory results within this range of values of M, α, and H; thus, additional FE analyses with intermediate values are not required. In addition, three idealized sand types, namely Loose Sand (LS), Medium Sand (MS), and Dense Sand (DS), have been examined and their mechanical properties are summarized in Table 1. In addition, the coefficient of lateral earth pressure at rest has been set equal to $K_0 = (1 - \sin\varphi)$, whereas for simplicity, drained conditions have been considered and the soil cohesion is equal to zero [83,84].

Table 1. Soil layer properties.

Sand Type	Soil Density (t/m^3)	Elastic Modulus ^{1} (MPa)	Friction Angle φ_p–φ_{res} (°)	Dilation Angle ψ_p–ψ_{res} (°)
Loose	1.6	$5 + 0.75 \cdot z$	30	0
Medium	1.8	$10 + 1.5 \cdot z$	34–30	6–0
Dense	2.0	$20 + 3 \cdot z$	39–30	11–0

^{1} Varying with respect to soil depth, z.

A continuous (i.e., with welded joints) steel gas pipeline of infinite length (i.e., a few kilometers long) has been examined with realistic cross-section dimensions: diameter, D = 0.9144 m (36 in), and thickness, t = 19.05 mm (0.75 in), and thus, ratio, D/t = 48, and pipe burial depth, H_b = 2 m. The pipe steel material is characterized by the API 5L X65 steel grade with Ramberg—Osgood plasticity, as follows:

$$\varepsilon = \frac{\sigma}{E} + \frac{\alpha_r \sigma_0}{E}\left(\frac{\sigma}{\sigma_0}\right) \tag{7}$$

where Young's Modulus, E = 210 GPa; Poissons' ratio, v = 0.3; yield stress, σ_0 = 490 MPa; hardening exponent, n = 20; and yield offset, α_r = 1.0. In addition, an external pipe coating corresponding to smooth steel has been used, i.e., related coefficient is set equal to 0.7.

In order to numerically simulate the problem of fault–pipe intersection via the decoupled numerical approach, the first FE model produces the PGDs, which have been subsequently imposed on the pipeline in the second FE model. Hence, the second FE model provides pipe distress in terms of strains (i.e., tensile, ε_t, and compressive, ε_c) at the top or bottom of the pipe cross-section, due to the combined axial loading and bending due to fault rupture propagation and potential outcropping. It is noted that the maximum tensile strain is the maximum positive strain, whereas the maximum compressive strain is the maximum absolute negative strain. Certainly, compressive strains are more critical as they can cause buckling of thin steel pipelines. Additionally, the case where the pipeline is (rather unrealistically) laid directly on the bedrock has been simulated for comparison with the results corresponding to various soil conditions. Finally, it is worth noticing that the worst-case scenario has been examined, i.e., by considering an unpressurized pipeline (internal pressure is set equal to 0 kPa).

The following graphs present indicative results from the detailed parametric investigation that has been performed. In particular, Figure 7 displays the impact of overlying soil properties on fault rupture propagation and outcropping, by means of plastic deformations. Figure 8a presents the resulting displacement profiles in terms of the ratio x/H, where x denotes the location along the horizontal axis of the FE soil model. The vertical axis indicates the total displacement, d, which has been calculated by means of the differential horizontal

and vertical displacements, *dx* and *dy*, respectively, by: $d = \sqrt{dx^2 + dy^2}$. Figure 8b depicts the impact of different overlying soil types on the resulting compressive strains of the pipeline.
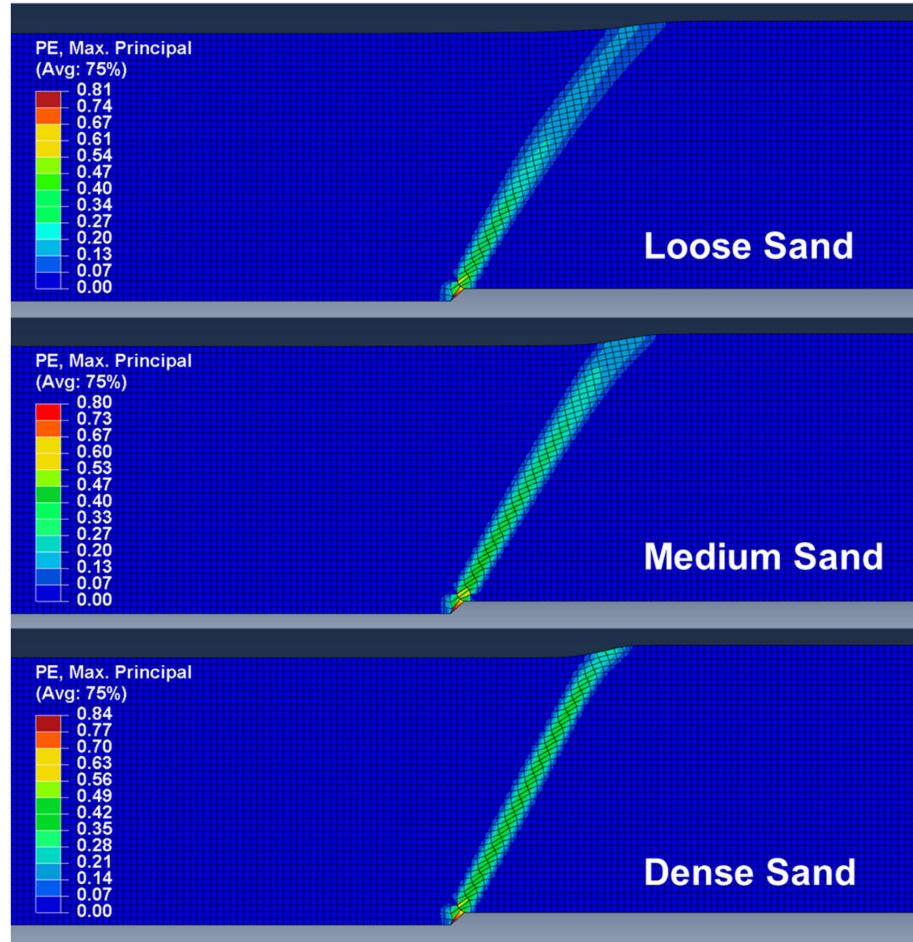
Figure 7. FE results of fault rupture, fault rupture propagation, and fault outcropping.

(**a**)   (**b**)
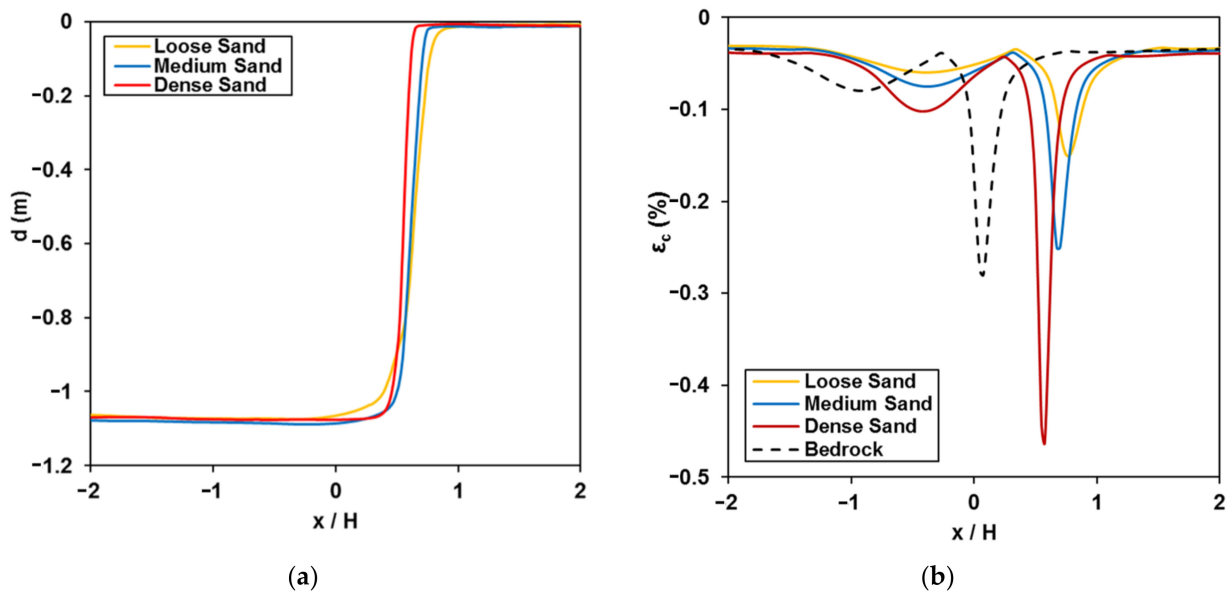
Figure 8. Impact of soil properties on: (**a**) the PGDs at the surface; (**b**) pipe compressive strains.

Two databases have been developed from the input and the output values of the numerical analyses for both FE models, namely a "geotechnical database" and a "structural database", in the form of 108×6 and 108×4 matrices, respectively. In both matrices, the 108 rows contain the data and the results of the conducted numerical analyses for all the cases examined for various combinations of input variables values, i.e., 108 in total. As far as the "geotechnical database" is concerned, the six columns of the matrix represent the soil layer thickness ($H = 0, 20, 50, 100$ m), the fault dip angle ($\alpha = 30°, 45°, 60°$) the sand type (LS, MS, DS), the earthquake magnitude ($M = 6.5, 7.0, 7.5$), and the resulting PGDs along the surface scarp, i.e., the absolute maximum horizontal and vertical differential displacements, dx and dy, respectively. Regarding the "structural database", the first two columns of the matrix are related to the PGDs in terms of maximum dx and dy at the surface, as computed from the numerical simulations, while the remaining columns list the resulting pipe deformations, in terms of maximum tensile, ε_t, and absolute maximum compressive, ε_c, strains.

Two shallow FFNNs (i.e., FFNN1 and FFNN2) have been generated to implement the proposed decoupled metamodel approach, using as input variables the first four columns of the "geotechnical database" and the first two of the "structural database", respectively, whereas the remaining two columns from each database have been utilized as target parameters. Table 2 summarizes the input and target parameters for each FFNN. It is noted that during the configuration (and subsequent cross-validation) of the structural FFNN (FFNN2), the input values (dx and dy) are those obtained from FEM calculations, not those predicted by FFNN1. On the other hand, when examining new data (i.e., not included in the available results of the FEM models) during the actual application of the developed metamodels, the FFNN1 predictions of dx and dy values will be used as the input of the second metamodel (FFNN2). Obviously, the two metamodels can also be utilized separately, e.g., if dx and dy are known from an experimental study, then only FFNN2 can be applied.

Table 2. Input and target parameters of the developed FFNNs for the two parts of the decoupled approach.

	FFNN1 (Geotechnical)	FFNN2 (Structural)
Input parameters	H, α, Sand type, M	max dx, max dy
Target parameters	max dx, max dy	max ε_t, max ε_c

Several different configurations have been tested for each network, while as aforementioned, the training process has been repeated 30 times for each ANN architecture and the statistical results are presented in the sequence. The LM and the BR training algorithms have been utilized, whereas a hidden layer consisting of 10, 25, and 50 hidden neurons has been selected. Note that for the FFNN2, which has only two input parameters, a hidden layer of five hidden neurons has been additionally examined as the input parameters are less compared to FFNN1 [78]. Furthermore, a more complex FFNN, consisting of two hidden layers, has been created from the "structural database", to increase the efficiency of the ANN-based metamodel for the problem of fault–pipe intersection. Hence, a variety of combinations between the number of hidden neurons per layer have been tested (i.e., 5×10, 10×5, 10×10, 10×25, 10×50, 25×10, 25×25, and 50×10).

As mentioned earlier, the performance of the FFNNs has been assessed via RMSE and R^2. Figures 9 and 10 depict these metrics for an indicative architecture for FFNN1 and FFNN2, respectively. Furthermore, Tables 3–5 summarize the main statistical variables regarding the output of the NNs for each of the examined configurations as derived from all training sessions. In addition, the regression plots in Figures 11 and 12a,b demonstrate the network predictions in terms of the actual values of FFNN1 and FFNN2, respectively. Lastly, Figures 13–15 present an interesting comparison regarding the duration of training sessions for both training algorithms and most of the developed architectures.
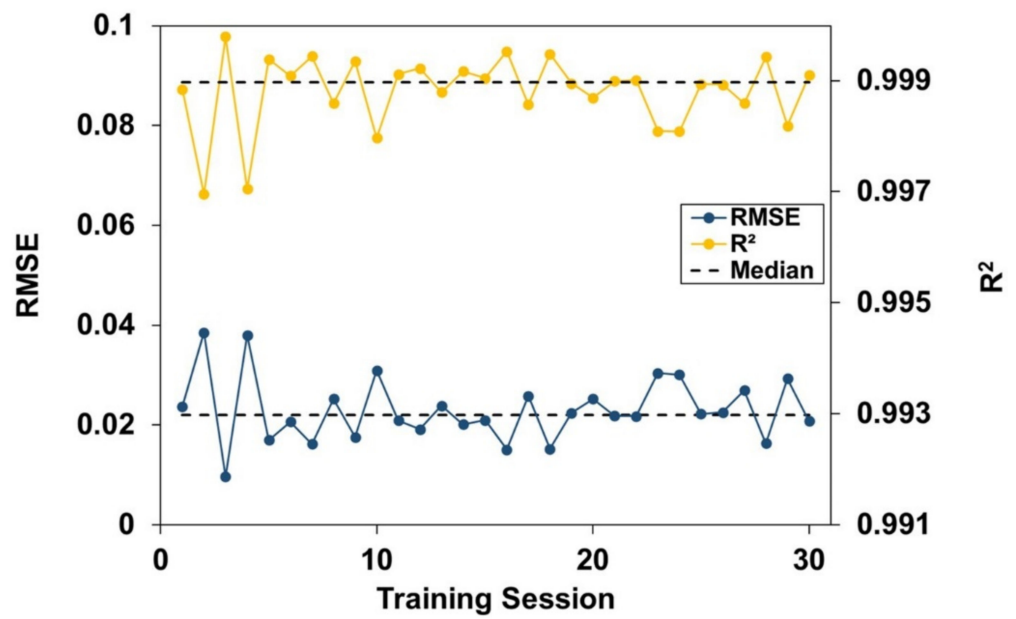
Figure 9. Performance metrics of the BR-trained FFNN1 consisting of 50 hidden neurons.
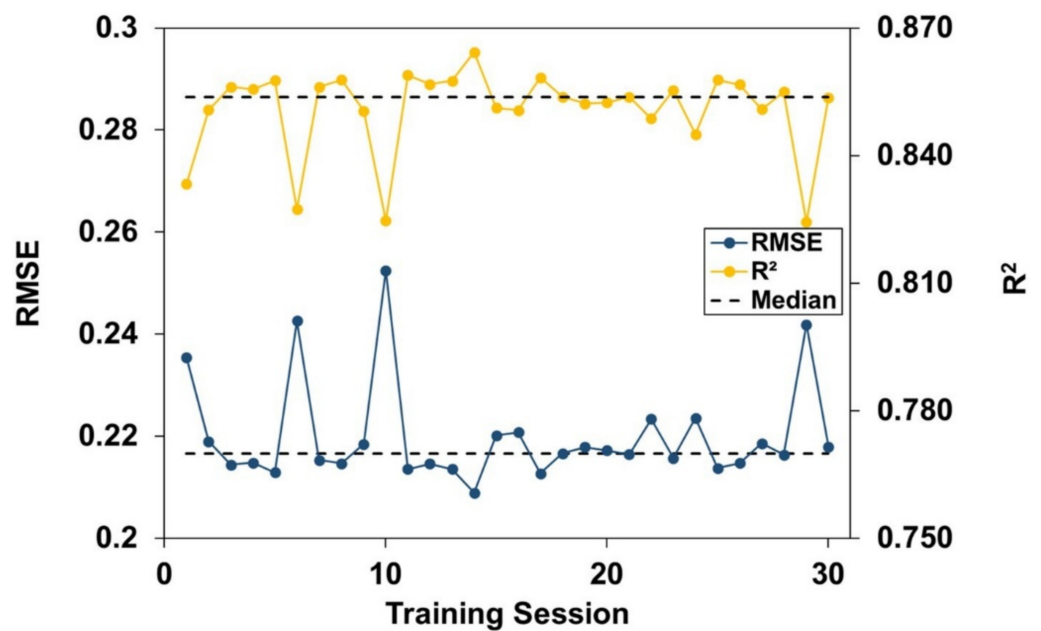
Figure 10. Performance metrics of the BR-trained FFNN2 consisting of 50 hidden neurons.

Table 3. Results summary for the geotechnical FFNN1.

Architecture	Statistical Variables	RMSE	R^2
LM—10 Hidden Neurons	Median	0.03698	0.99695
	Standard Deviation	0.02278	0.00539
	Max	0.09797	0.99876
	Min	0.02324	0.97904
BR—10 Hidden Neurons	Median	0.02262	0.99885
	Standard Deviation	0.00204	0.00020
	Max	0.02784	0.99916
	Min	0.01905	0.99831

Table 3. *Cont.*

Architecture	Statistical Variables	RMSE	R^2
LM—25 Hidden Neurons	Median	0.04153	0.99610
	Standard Deviation	0.02235	0.00569
	Max	0.10206	0.99855
	Min	0.02463	0.97917
BR—25 Hidden Neurons	Median	0.02334	0.99885
	Standard Deviation	0.00688	0.00081
	Max	0.04677	0.99962
	Min	0.01297	0.99542
LM—50 Hidden Neurons	Median	0.15587	0.95146
	Standard Deviation	0.04422	0.03045
	Max	0.28601	0.98646
	Min	0.07902	0.84409
BR—50 Hidden Neurons	Median	0.02205	0.99897
	Standard Deviation	0.00646	0.00067
	Max	0.03853	0.99979
	Min	0.00969	0.99696

Table 4. Results summary for the structural FFNN2 with one hidden layer.

Architecture	Statistical Variables	RMSE	R^2
LM—5 Hidden Neurons	Median	0.27155	0.78168
	Standard Deviation	0.04859	0.04432
	Max	0.45701	0.85027
	Min	0.21981	0.68250
BR—5 Hidden Neurons	Median	0.29566	0.72811
	Standard Deviation	0.00278	0.00511
	Max	0.29879	0.75549
	Min	0.28145	0.72533
LM—10 Hidden Neurons	Median	0.23587	0.83134
	Standard Deviation	0.04046	0.05297
	Max	0.35286	0.87156
	Min	0.20347	0.64175
BR—10 Hidden Neurons	Median	0.29587	0.72799
	Standard Deviation	0.01386	0.02695
	Max	0.29916	0.83781
	Min	0.22979	0.72135
LM—25 Hidden Neurons	Median	0.24025	0.83521
	Standard Deviation	0.05237	0.08218
	Max	0.40672	0.86591
	Min	0.20778	0.52519
BR—25 Hidden Neurons	Median	0.22004	0.85013
	Standard Deviation	0.02441	0.03798
	Max	0.30105	0.85634
	Min	0.21514	0.72450
LM—50 Hidden Neurons	Median	0.24151	0.81832
	Standard Deviation	0.05512	0.06510
	Max	0.38717	0.90133
	Min	0.17772	0.63919
BR—50 Hidden Neurons	Median	0.21655	0.85377
	Standard Deviation	0.00999	0.01015
	Max	0.25247	0.86430
	Min	0.20890	0.82439

Table 5. Results summary for the structural FFNN2 with two hidden layers.

Architecture	Statistical Variables	RMSE	R^2
LM—5 × 10 Hidden Neurons	Median	0.26565	0.82506
	Standard Deviation	0.05739	0.04323
	Max	0.47187	0.88050
	Min	0.21242	0.72356
BR—5 × 10 Hidden Neurons	Median	0.29571	0.76856
	Standard Deviation	0.02252	0.03180
	Max	0.29722	0.88047
	Min	0.21246	0.76587
LM—10 × 5 Hidden Neurons	Median	0.23103	0.86412
	Standard Deviation	0.03109	0.04338
	Max	0.34773	0.90018
	Min	0.19409	0.68232
BR—10 × 5 Hidden Neurons	Median	0.29513	0.76904
	Standard Deviation	0.03057	0.03993
	Max	0.30058	0.90850
	Min	0.18706	0.76318
LM—10 × 10 Hidden Neurons	Median	0.25370	0.83276
	Standard Deviation	0.05271	0.04883
	Max	0.42663	0.93434
	Min	0.15752	0.71802
BR—10 × 10 Hidden Neurons	Median	0.29577	0.76843
	Standard Deviation	0.00151	0.00172
	Max	0.30071	0.76963
	Min	0.29467	0.76257
LM—10 × 25 Hidden Neurons	Median	0.23298	0.86119
	Standard Deviation	0.06378	0.06466
	Max	0.43960	0.94042
	Min	0.14983	0.65386
BR—10 × 25 Hidden Neurons	Median	0.29586	0.76807
	Standard Deviation	0.02948	0.03941
	Max	0.37691	0.87892
	Min	0.21367	0.66373
LM—25 × 10 Hidden Neurons	Median	0.24362	0.84878
	Standard Deviation	0.10106	0.06233
	Max	0.75498	0.90155
	Min	0.19536	0.63703
BR—25 × 10 Hidden Neurons	Median	0.29542	0.76880
	Standard Deviation	0.00126	0.00159
	Max	0.29925	0.76983
	Min	0.29438	0.76335
LM—25 × 25 Hidden Neurons	Median	0.24299	0.85201
	Standard Deviation	0.09679	0.10996
	Max	0.55564	0.89903
	Min	0.19498	0.32879
BR—25 × 25 Hidden Neurons	Median	0.29525	0.76875
	Standard Deviation	0.02397	0.03263
	Max	0.29890	0.87516
	Min	0.21697	0.76328

Table 5. *Cont.*

Architecture	Statistical Variables	RMSE	R^2
LM—50 × 10 Hidden Neurons	Median	0.23846	0.86035
	Standard Deviation	0.06901	0.09167
	Max	0.46603	0.92467
	Min	0.17090	0.47852
BR—50 × 10 Hidden Neurons	Median	0.21545	0.87729
	Standard Deviation	0.03271	0.04266
	Max	0.30066	0.93083
	Min	0.16150	0.75999
LM—10 × 50 Hidden Neurons	Median	0.23592	0.85442
	Standard Deviation	0.07041	0.07959
	Max	0.49993	0.90093
	Min	0.19422	0.57819
BR—10 × 50 Hidden Neurons	Median	0.29554	0.76844
	Standard Deviation	0.01753	0.02313
	Max	0.29964	0.89289
	Min	0.20085	0.76273
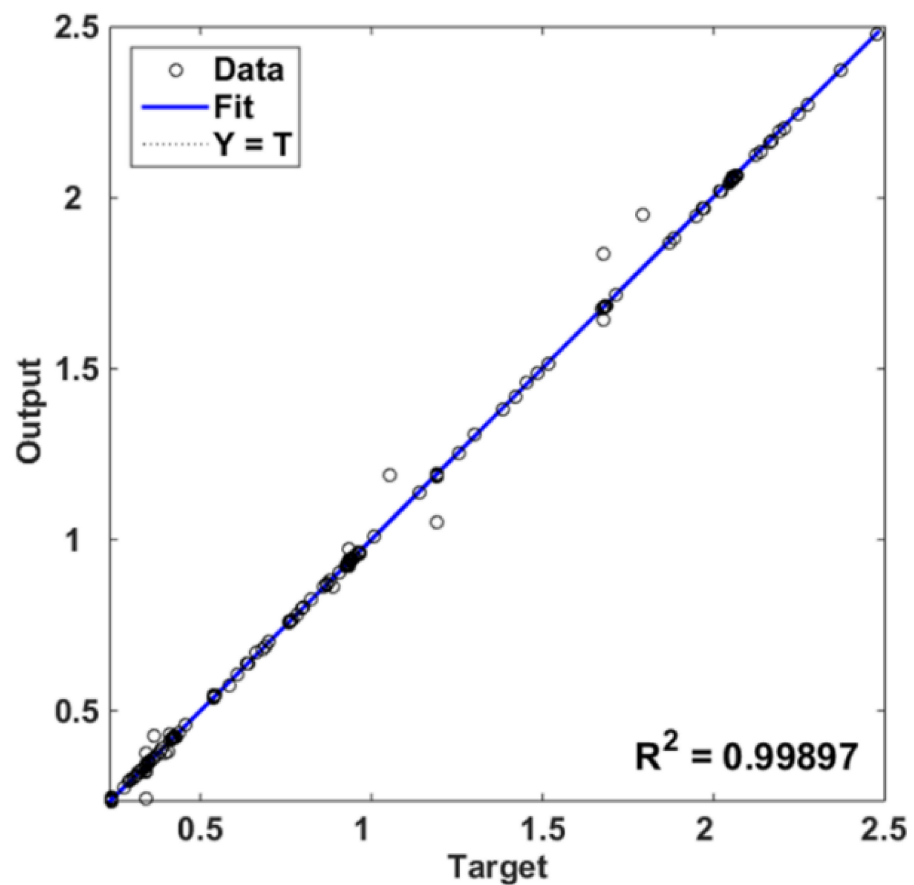
Figure 11. Regression plot of FFNN1 with BR and 50 hidden neurons.

(**a**)   (**b**)
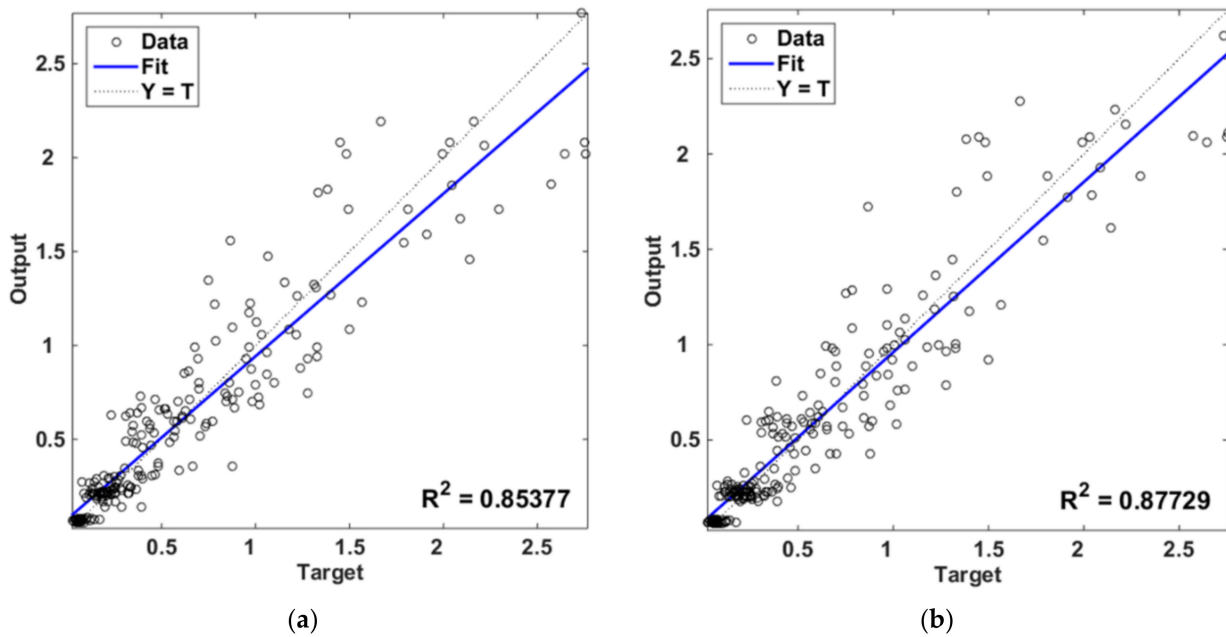
Figure 12. Regression plots of FFNN2 with BR and: (**a**) a single hidden layer having 50 neurons; (**b**) two hidden layers having 50×10 neurons.

(**a**)   (**b**)
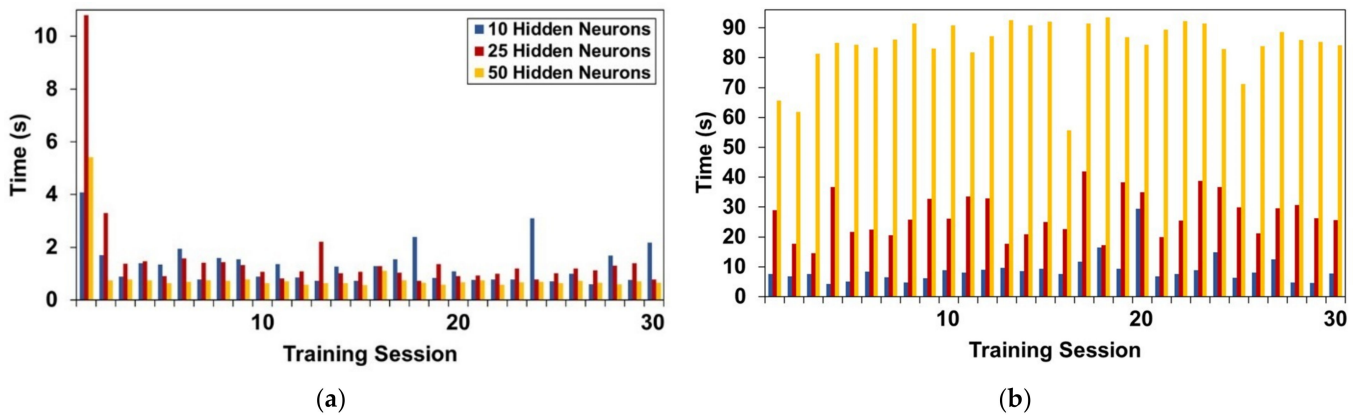
Figure 13. Duration of each training session of FFNN1 for: (**a**) LM training algorithm; (**b**) BR training algorithm.

(**a**)   (**b**)
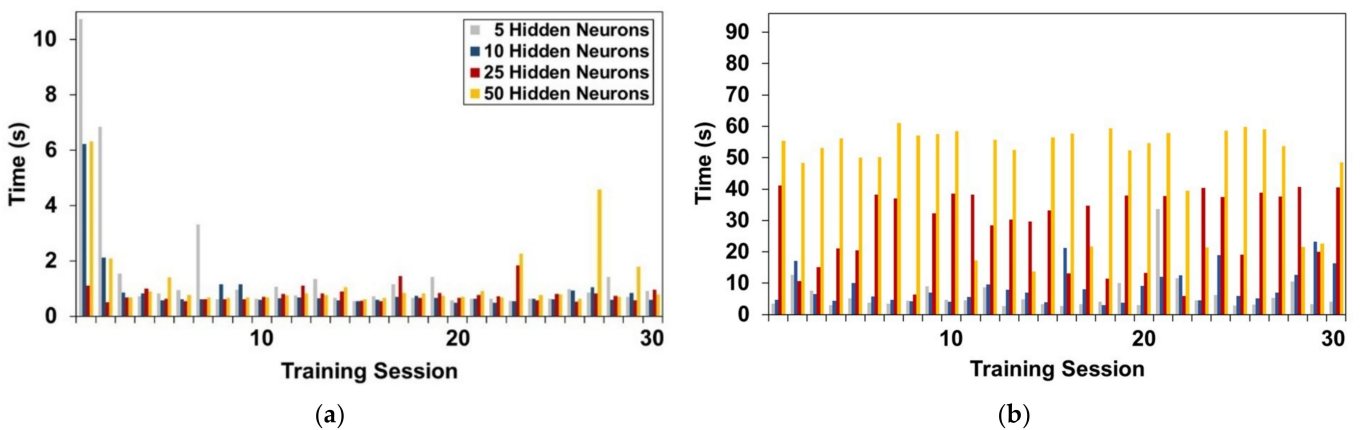
Figure 14. Duration of each training session of FFNN2 with a single hidden layer for: (**a**) LM training algorithm; (**b**) BR training algorithm.
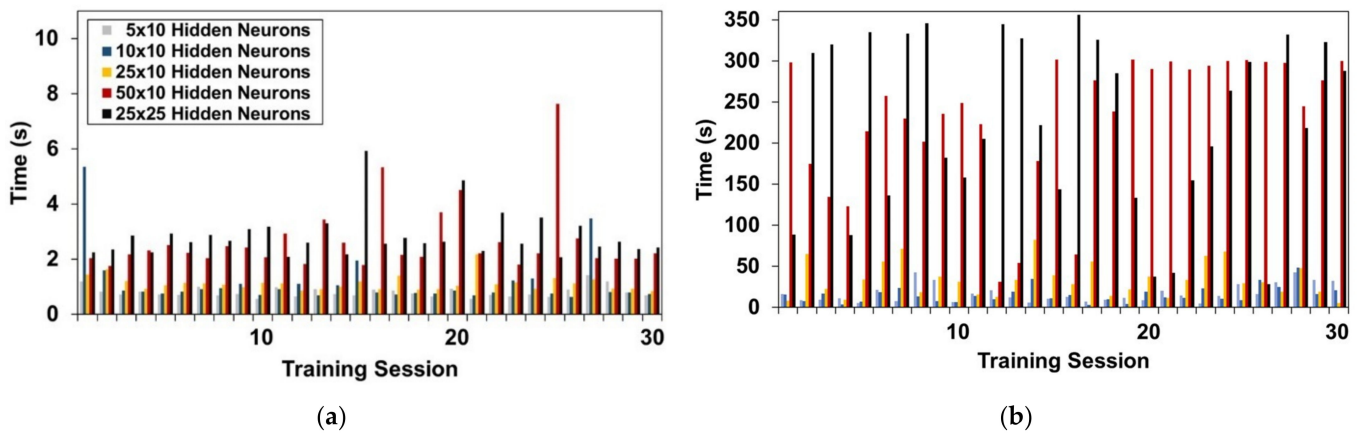
Figure 15. Duration of each training session of FFNN2 with two hidden layers for: (**a**) LM training algorithm; (**b**) BR training algorithm.

Taking into account that the testing subset can be re-used for training and validation in another training session, an additional cross-validation of the predictions of the developed networks has been performed to verify their efficiency. The prediction capability and accuracy of both metamodels (i.e., the ones that present the median performance values) is assessed using new data that have not been used during the development of the metamodels. Accordingly, an additional analysis set has been conducted in ABAQUS software after completing the training process. More specifically, two FE models (for the soil response and fault–pipe intersection) have previously been developed, corresponding to the following data: $H = 50$ m, $\alpha = 50°$, DS soil type, and $M = 7.5$. It is noted that the selected data are within the range of the input values that have fed the NNs. The corresponding results, in terms of PGDs and pipe strains, have been compared with the predictions of the geotechnical and structural surrogate metamodels, respectively. Tables 6–8 summarize this comparison, presenting the associated errors between FEM and FFNNs.

Table 6. Comparison between NN and FEM results of FFNN1.

Hidden Neurons	Training Algorithm	Abaqus *dx/dy*	FFNN *dx/dy*	Error (%) *dx/dy*
10	LM		1.55/2.19	2.15/2.71
	BR		1.58/2.21	3.91/1.73
25	LM	1.52/2.25	1.53/2.23	0.93/0.89
	BR		1.54/2.22	1.61/1.63
50	LM		1.51/2.26	0.71/0.09
	BR		1.54/2.26	1.47/0.41

Table 7. Comparison between NN predictions and FEM results of FFNN2 with one hidden layer.

Hidden Neurons	Training Algorithm	Abaqus $\varepsilon_t/\varepsilon_c$	FFNN $\varepsilon_t/\varepsilon_c$	Error (%) $\varepsilon_t/\varepsilon_c$
5	LM		1.83/0.85	14.57/16.51
	BR		1.71/0.80	20.30/21.56
10	LM		1.83/0.87	14.67/14.35
	BR		1.71/0.80	20.02/21.27
25	LM	2.14/1.02	2.05/0.90	4.13/11.81
	BR		1.83/0.87	14.47/14.68
50	LM		2.26/1.00	5.87/1.93
	BR		1.86/0.88	13.07/14.17

Table 8. Comparison between NN predictions and FEM results of FFNN2 with two hidden layers.

Hidden Neurons	Training Algorithm	Abaqus $\varepsilon_t/\varepsilon_c$	FFNN $\varepsilon_t/\varepsilon_c$	Error (%) $\varepsilon_t/\varepsilon_c$
5 × 10	LM		1.80/0.87	15.62/14.58
	BR		1.70/0.80	20.37/21.59
10 × 5	LM		1.87/0.90	12.59/12.09
	BR		1.71/0.81	19.91/21.12
10 × 10	LM		1.95/0.87	9.00/14.66
	BR		1.71/0.80	20.11/21.36
10 × 25	LM		2.00/0.87	6.72/14.73
	BR		1.71/0.80	20.04/21.32
25 × 10	LM	2.14/1.02	2.07/0.87	3.39/14.47
	BR		1.70/0.80	20.49/21.71
25 × 25	LM		2.09/0.97	2.32/5.46
	BR		1.71/0.80	20.15/21.22
50 × 10	LM		2.17/1.01	1.56/1.10
	BR		1.87/0.88	12.62/13.40
10 × 50	LM		1.96/0.80	8.23/22.04
	BR		1.71/0.81	20.00/21.19

4. Discussion

The results presented in Figures 7 and 8a reveal that the material properties of the overlying soil stratum have a critical impact on the fault rupture propagation paths, thus confirming the findings of relevant studies (e.g., [85]). More specifically, Figure 7 demonstrates that fault rupture has led to fully-developed failure patterns that tend to diverge from the straight projection of the fault dip, regardless of sand type. This trend is in agreement with the studies of Loukidis et al. [86] and Thebian et al. [70]. Figures 7 and 8a illustrate that LS has resulted in wider shear rupture zones and smoother displacement profiles compared to MS and DS soil types. This can be attributed to the fact that LS is characterized by higher levels of elastic deformation, which are related to the lower stiffness and the higher ductile "macroscopic" behavior compared to DS and MS, as reported in related numerical and experimental studies (e.g., [67,68,87])

Accordingly, Figure 8b indicates that a soft soil layer (consisting of LS) may have a beneficial impact on the structural response of buried pipelines, since lower absolute values of compressive strains have been derived compared to stiffer sandy soils (MS and DS). This observation is in agreement with the study of Özcebe et al. [88] and is attributed to the aforementioned characteristics of LS. Figure 8b presents an additional comparison by including the case where the pipeline is directly laid on bedrock. In contrast to DS, where the pipeline has developed larger compressive strains than "Bedrock", LS significantly reduced the resulting pipe deformation; thus, it can be seen as an efficient mitigation measure in real-life projects. More details regarding the impact of soil properties and several critical factors on the phenomenon of fault rupture propagation, as well as on the problem of fault–pipe intersection, are presented in Makrakis et al. [24,25].

Results from Tables 3–5 indicate that the geotechnical FFNN (i.e., FFNN1) has produced better results compared to the structural FFNN (i.e., FFNN2). More specifically, Table 3 illustrates that all the examined configurations of FFNN1 for both training algorithms and number of hidden neurons have produced satisfactory results, since the corresponding median values of RMSE and R^2 are close to 0 and 1, respectively. The FFNN1 consisting of 50 hidden neurons and trained with the LM algorithm exhibits less satisfactory performance than the other configurations, as it has resulted in larger RMSE and lower R^2.

Conversely, the BR training algorithm is generally superior to LM. In addition, it has been revealed that a substantial increase of the number of hidden neurons (i.e., from 10 to 50) has a significant impact on the training duration of the BR-trained network, leading on

average almost to ten-times longer training time, without any considerable change on the corresponding evaluation metrics. On the other hand, increasing the number of hidden neurons in LM has marginal impact on the training duration.

Table 4 shows that increasing the number of hidden neurons of FFNN2 with a single layer has a beneficial impact on the performance metrics of the BR-trained networks. With respect to LM training algorithm, changing the architecture of the network does not affect the results, as similar values of both RMSE and R^2 can be seen for the 5, 10, 25, and 50 hidden neurons. Note that the training duration of the BR-trained network consisting of 50 hidden neurons is notably lower compared to the same architecture of FFNN1. However, the fact that the obtained results of FFNN2 are not characterized by a strong linear relationship between the predicted and the target values (i.e., values of R^2 are not close enough to 1) has led to the development of a more complex FFNN2 with two hidden layers.

Results in Table 5 indicate that increasing the number of hidden layers does not lead to better performance metrics, regardless of training algorithm and neurons combinations in the two hidden layers, thus confirming the findings of Cho et al. [58]. However, it is mentioned that the BR-trained FFNN2 consisting of 25 × 25, as well as 50 × 10 hidden neurons per hidden layer, has resulted in 5-times and 90-times increase of training duration compared to the BR-trained FFNN2 with a single layer having 50 neurons and the LM-trained FFNN2 with 25 × 25 and 50 × 10 hidden neurons, respectively.

Regarding the comparison between FEM results and NN predictions in the cross-validation of the developed networks, Table 6 indicates the high-level predictive capabilities of the geotechnical FFNN when using data that have not been previously involved in the FFNN1 training process. In particular, the corresponding errors range between 0.09% and 3.91%, for all the examined training algorithms and numbers of hidden neurons. In contrast, as presented in Table 7, FFNN2 exhibits much higher prediction errors, i.e., >10% in most cases. The LM-trained network consisting of a single layer having 50 neurons exhibits quite acceptable prediction errors, i.e., slightly lower than 6% and 2% for ε_t and ε_c, respectively. Similarly, Table 8 shows that the FFNN2 with two hidden layers has not led to a notable reduction of the prediction errors. However, the LM-trained network consisting of 50 × 10 hidden neurons has reduced the prediction errors to 1.6% and 1.1% for ε_t and ε_c, respectively; thus, it has very good prediction capability.

Finally, it has to be stressed that the predictions of all metamodels are obtained in a fraction of time compared to the time needed for the actual FEM analyses, which need several minutes for the examined case studies, especially the ones related to the calculations of pipeline distress.

5. Conclusions

Although ANNs have been successfully applied in various engineering fields, they have not been used in infrastructure geotechnics and in particular in the earthquake-related geohazard of fault rupture and the resulting distress of lifelines. Therefore, this critical issue with direct practical importance, as it is related with the seismic design and route optimization of buried gas pipelines, has been examined herein. More specifically, the current study presents the results of: (i) a numerical investigation regarding the phenomena of fault rupture and fault rupture propagation through a sandy soil layer, as well as the associated problem of fault–pipe intersection, and (ii) a detailed sensitivity analysis related to the optimal application of ANN-based on these problems.

The numerical simulations have been carried out by employing a decoupled FE methodology, i.e., by developing separate models for the surrounding soil and the pipeline distress. The data of a detailed parametric investigation have been used, considering dip-slip faulting with different dip angles and loading conditions (i.e., earthquake magnitudes), while a sandy soil layer of varying thickness and mechanical properties has been considered. The soil displacement profile, in terms of PGDs, as well as the pipeline deformation, in terms of strains, have been derived. Based on the input and output data of this parametric investigation, two separate ANN-based metamodels have been developed as an efficient

alternative to the time-consuming FEM analyses, aiming to facilitate the fast and reliable assessment of PGDs and pipeline structural performance due to tectonic faulting.

Based on the presented results, the following conclusions can be drawn:

- The overlying soil stratum may have a critical impact on the fault rupture propagation paths, leading to fully-developed failure patterns up to the ground surface. In addition, the presence of the soil layer may affect the structural performance of buried gas pipelines in a beneficial or even a detrimental manner, compared to the case where the pipeline is directly laid on bedrock.

- The developed geotechnical FFNN (FFNN1), which focuses on surface PGDs due to seismic fault rupture, has produced satisfactory predictions, since RMSE and R^2 are close to 0 and 1, respectively, for all the examined architectures and training algorithms. BR-trained FFNN1 exhibits a better overall performance compared to LM-trained. A marginal impact on the training duration has been reported from the increase of hidden neurons in LM, whereas increasing the number of hidden neurons has led to slightly better results, but significantly longer training duration for BR-trained networks.

- The developed structural metamodel (FFNN2) exhibits worse performance metrics than FFNN1. The BR-trained single hidden layer network consisting of 50 neurons outperforms the other schemes. Similarly to FFNN1, the increase on the number of hidden neurons has affected only the training duration and performance of the BR-trained network. Increasing the number of hidden layers of FFNN2 has not improved much the performance metrics, regardless of training algorithm and number of neurons per hidden layer.

- Regarding the cross-validation with new data, FFNN1 is characterized by exceptional predictive performance for independent data, leading to 0.71% and 0.09% prediction errors for *dx* and *dy*, respectively. Conversely, FFNN2 has generally resulted in prediction errors greater than 10%. However, the LM-trained FFNN2 with a single hidden layer having 50 neurons resulted in errors slightly lower than 6% and 2% for ε_t and ε_c, respectively. Although the use of two hidden layers in FFNN2 has not led to a notable reduction of the prediction errors, the LM-trained network consisting of 50×10 hidden neurons has resulted in acceptable prediction errors, i.e., 1.6% and 1.1% for ε_t and ε_c, respectively.

Summarizing, the main advantage of the developed metamodels is that they can efficiently replace time-consuming FEM analyses, while the time and effort required for pre- and post-processing of FEM models are also avoided. On the other hand, the training process is not a straightforward task, as fine-tuning and optimization of ANN configuration requires adequate experience. Nonetheless, on the basis of the promising findings presented in this work, further investigations can be performed taking into account soil cohesion and wet conditions, the presence of multi-layered soil deposits, as well as three-dimensional finite elements for the more accurate representation of the structural response of the pipeline. Regarding the application of Artificial Intelligence methods in the examined problems, larger training datasets should be created, and different training algorithms and networks with more complex structure could be examined, such as Regression and Convolutional Neural Networks, in which the whole profile of ground deformations could be used.

Author Contributions: Conceptualization, N.M., P.N.P. and Y.T.; methodology, N.M., P.N.P. and Y.T.; software, N.M.; validation, N.M.; formal analysis, N.M. and Y.T.; investigation, N.M., P.N.P. and Y.T.; resources, N.M., P.N.P. and Y.T.; data curation, N.M.; writing—original draft preparation, N.M., P.N.P. and Y.T.; writing—review and editing, N.M., P.N.P. and Y.T.; visualization, N.M., P.N.P. and Y.T.; supervision, Y.T.; project administration, Y.T. All authors have read and agreed to the published version of the manuscript.

Data Availability Statement: Not applicable.

Conflicts of Interest: The authors declare no conflict of interest. None of the funders had any role in the design of the study; in the collection, analyses, or interpretation of data; in the writing of the manuscript, or in the decision to publish the results.

References

1. Nair, G.S.; Dash, S.R.; Mondal, G. Review of Pipeline Performance during Earthquakes since 1906. *J. Perform. Constr. Facil.* **2018**, *32*, 04018083. [CrossRef]
2. Newmark, N.M.; Hall, W.J. Pipeline Design to Resist Large Fault Displacement. In *Proceedings of US National Conference on Earthquake Engineering*; Earthquake Engineering Research Institute: Oakland, CA, USA, 1975.
3. Kennedy, R.P.; Chow, A.M.; Williamson, R.A. Fault Movement Effects on Burried Oil Pipeline. *ASCE Transp. Eng. J.* **1977**, *103*, 617–633. [CrossRef]
4. Wang, L.R.; Yeh, Y.-H. A Refined Seismic Analysis and Design of Buried Pipeline for Fault Movement. *Earthq. Eng. Struct. Dyn.* **1985**, *13*, 75–96. [CrossRef]
5. Jalali, H.H.; Rofooei, F.R.; Khajeh, A.A.N. Performance of Buried Gas Distribution Pipelines Subjected to Reverse Fault Movement. *J. Earthq. Eng.* **2018**, *22*, 1068–1091. [CrossRef]
6. Tsatsis, A.; Loli, M.; Gazetas, G. Pipeline in Dense Sand Subjected to Tectonic Deformation from Normal or Reverse Faulting. *Soil Dyn. Earthq. Eng.* **2019**, *127*, 105780. [CrossRef]
7. Fadaee, M.; Farzaneganpour, F.; Anastasopoulos, I. Response of Buried Pipeline Subjected to Reverse Faulting. *Soil Dyn. Earthq. Eng.* **2020**, *132*, 106090. [CrossRef]
8. Dey, S.; Chakraborty, S.; Tesfamariam, S. Structural Performance of Buried Pipeline Undergoing Strike-Slip Fault Rupture in 3D Using a Non-Linear Sand Model. *Soil Dyn. Earthq. Eng.* **2020**, *135*, 106180. [CrossRef]
9. Joshi, S.; Prashant, A.; Deb, A.; Jain, S.K. Analysis of Buried Pipelines Subjected to Reverse Fault Motion. *Soil Dyn. Earthq. Eng.* **2011**, *31*, 930–940. [CrossRef]
10. Uckan, E.; Akbas, B.; Shen, J.; Rou, W.; Paolacci, F.; O'Rourke, M. A Simplified Analysis Model for Determining the Seismic Response of Buried Steel Pipes at Strike-Slip Fault Crossings. *Soil Dyn. Earthq. Eng.* **2015**, *75*, 55–65. [CrossRef]
11. Chatzidakis, D.; Tsompanakis, Y.; Psarropoulos, P.N. Kinematic Distress of Pipelines Subjected to Secondary Seismic Fault Rupture. *Soil Dyn. Earthq. Eng.* **2022**, *152*, 107065. [CrossRef]
12. Makrakis, N.; Psarropoulos, P.N.; Sextos, A.; Tsompanakis, Y. Quantifying the Impact of Soft Surface Soil Layers on Fault Rupture Propagation and Kinematic Distress of Offshore and Onshore Pipelines. In Proceedings of the 17th International Pipeline Technology Conference (PTC), Berlin, Germany, 7–10 March 2022.
13. Karamitros, D.K.; Bouckovalas, G.D.; Kouretzis, G.P. Stress Analysis of Buried Steel Pipelines at Strike-Slip Fault Crossings. *Soil Dyn. Earthq. Eng.* **2007**, *27*, 200–211. [CrossRef]
14. Trifonov, O.V.; Cherniy, V.P. Elastoplastic Stress-Strain Analysis of Buried Steel Pipelines Subjected to Fault Displacements with Account for Service Loads. *Soil Dyn. Earthq. Eng.* **2012**, *33*, 54–62. [CrossRef]
15. Sarvanis, G.C.; Karamanos, S.A. Analytical Model for the Strain Analysis of Continuous Buried Pipelines in Geohazard Areas. *Eng. Struct.* **2017**, *152*, 57–69. [CrossRef]
16. Sarvanis, G.C.; Karamanos, S.A.; Vazouras, P.; Mecozzi, E.; Lucci, A.; Dakoulas, P. Permanent Earthquake-Induced Actions in Buried Pipelines: Numerical Modeling and Experimental Verification. *Earthq. Eng. Struct. Dyn.* **2018**, *47*, 966–987. [CrossRef]
17. Psyrras, N.; Sextos, A.; Crewe, A.; Dietz, M.; Mylonakis, G. Physical Modeling of the Seismic Response of Gas Pipelines in Laterally Inhomogeneous Soil. *J. Geotech. Geoenvironmental Eng.* **2020**, *146*, 04020031. [CrossRef]
18. Demirci, H.E.; Bhattacharya, S.; Karamitros, D.; Alexander, N. Experimental and Numerical Modelling of Buried Pipelines Crossing Reverse Faults. *Soil Dyn. Earthq. Eng.* **2018**, *114*, 198–214. [CrossRef]
19. Rojhani, M.; Moradi, M.; Galandarzadeh, A.; Takada, S. Centrifuge Modeling of Buried Continuous Pipelines Subjected to Reverse Faulting. *Can. Geotech. J.* **2012**, *49*, 659–670. [CrossRef]
20. Saiyar, M.; Ni, P.; Take, W.A.; Moore, I.D. Response of Pipelines of Differing Flexural Stiffness to Normal Faulting. *Geotechnique* **2016**, *66*, 275–286. [CrossRef]
21. American Society of Civil Engineers (ASCE); Committee on Gas and Liquid Fuel Lifelines. *Guidelines for the Seismic Design of Oil and Gas Pipeline Systems*; American Society of Civil Engineers: New York, NY, USA, 1984; ISBN 978-0-87262-428-3.
22. American Lifelines Alliance. *Guidelines for the Design of Buried Steel Pipe*; American Society of Civil Engineers: Reston, VA, USA, 2001.
23. *EN 1998-4:2006*; European Commitee for Standardization (CEN)—Eurocode 8: Design of Structures for Earthquake Resistance—Part 4: Silos, Tanks and Pipelines. European Commitee for Standardization: Brussels, Belgium, 2006.
24. Makrakis, N.; Psarropoulos, P.N.; Sextos, A.; Tsompanakis, Y. New Empirical Relationships for the Assessment of Soft Surface Soil Layers Impact on Fault-Rupture Propagation. 2022; *to be sumbitted*.
25. Makrakis, N.; Psarropoulos, P.N.; Sextos, A.; Tsompanakis, Y. Quantifying the Impact of Soft Soil Layers on the Kinematic Distress of Onshore High-Pressure Gas Pipelines. *Bull. Earthq. Eng.* **2022**. *under review*.
26. Lagaros, N.D.; Tsompanakis, Y. *Intelligent Computational Paradigms in Earthquake Engineering*; Lagaros, N.D., Tsompanakis, Y., Eds.; Idea Group Publishing, Inc.: Hershey, PA, USA, 2007; ISBN 9781599040998.

27. Das, S.K.; Kumar, A.; Das, B.; Burnwal, B. On Soft Computing Techniques in Various Areas. *Comput. Sci. Inf. Technol.* **2013**, *3*, 59–68. [CrossRef]

28. Sobhani, J.; Ramezanianpour, A.A. Service Life of the Reinforced Concrete Bridge Deck in Corrosive Environments: A Soft Computing System. *Appl. Soft Comput. J.* **2011**, *11*, 3333–3346. [CrossRef]

29. Chandwani, V.; Agrawal, V.; Nagar, R. Applications of Soft Computing in Civil Engineering: A Review. *Int. J. Comput. Appl.* **2013**, *81*, 00975–08887. [CrossRef]

30. Fister, I.; Gandomi, A.H.; Fister, I., Jr.; Mousavi, M.; Farhadi, A. Soft Computing in Earthquake Engineering: A Short Overview. *Int. J. Earthq. Eng. Hazard Mitig.* **2014**, *2*, 42–48.

31. Tsompanakis, Y.; Lagaros, N.D.; Stavroulakis, G.E. Soft Computing Techniques in Parameter Identification and Probabilistic Seismic Analysis of Structures. *Adv. Eng. Softw.* **2008**, *39*, 612–624. [CrossRef]

32. Salehi, H.; Burgueño, R. Emerging Artificial Intelligence Methods in Structural Engineering. *Eng. Struct.* **2018**, *171*, 170–189. [CrossRef]

33. Das, S.K.; Samui, P.; Sabat, A.K. Application of Artificial Intelligence to Maximum Dry Density and Unconfined Compressive Strength of Cement Stabilized Soil. *Geotech. Geol. Eng.* **2011**, *29*, 329–342. [CrossRef]

34. Kim, S.; Hwang, Y.; Seo, H.; Kim, B. Ground Motion Amplification Models for Japan Using Machine Learning Techniques. *Soil Dyn. Earthq. Eng.* **2020**, *132*, 106095. [CrossRef]

35. Gajan, S. Application of Machine Learning Algorithms to Performance Prediction of Rocking Shallow Foundations during Earthquake Loading. *Soil Dyn. Earthq. Eng.* **2021**, *151*, 106965. [CrossRef]

36. Zhang, Y.; Ge, T.; Tian, W.; Liou, Y.A. Debris Flow Susceptibility Mapping Using Machine-Learning Techniques in Shigatse Area, China. *Remote Sens.* **2019**, *11*, 2801. [CrossRef]

37. Ghorbanzadeh, O.; Blaschke, T.; Gholamnia, K.; Meena, S.R.; Tiede, D.; Aryal, J. Evaluation of Different Machine Learning Methods and Deep-Learning Convolutional Neural Networks for Landslide Detection. *Remote Sens.* **2019**, *11*, 196. [CrossRef]

38. Rahmati, O.; Falah, F.; Dayal, K.S.; Deo, R.C.; Mohammadi, F.; Biggs, T.; Moghaddam, D.D.; Naghibi, S.A.; Bui, D.T. Machine Learning Approaches for Spatial Modeling of Agricultural Droughts in the South-East Region of Queensland Australia. *Sci. Total Environ.* **2020**, *699*, 134230. [CrossRef]

39. Wagenaar, D.; Curran, A.; Balbi, M.; Bhardwaj, A.; Soden, R.; Hartato, E.; Mestav, S.G.; Ruangpan, L.; Molinario, G.; Lallemant, D. Invited Perspectives: How Machine Learning Will Change Flood Risk and Impact Assessment. *Nat. Hazards Earth Syst. Sci.* **2020**, *20*, 1149–1161. [CrossRef]

40. Ma, Z.; Mei, G. Deep Learning for Geological Hazards Analysis: Data, Models, Applications, and Opportunities. *Earth-Sci. Rev.* **2021**, *223*, 103858. [CrossRef]

41. McCulloch, W.S.; Pitts, W. A Logical Calculus of the Ideas Immanent in Nervous Activity. *Bull. Math. Biophys.* **1943**, *5*, 115–143. [CrossRef]

42. Nedic, V.; Despotovic, D.; Cvetanovic, S.; Despotovic, M.; Babic, S. Comparison of Classical Statistical Methods and Artificial Neural Network in Traffic Noise Prediction. *Environ. Impact Assess. Rev.* **2014**, *49*, 24–30. [CrossRef]

43. Haykin, S. *Neural Networks: A Comprehensive Foundation*, 2nd ed.; Pearson Prentice Hall: Noida, India, 2003; ISBN 8120323734.

44. Papadrakakis, M.; Lagaros, N.D.; Tsompanakis, Y. Structural Optimization Using Evolution Strategies and Neural Networks. *Comput. Methods Appl. Mech. Eng.* **1998**, *156*, 309–333. [CrossRef]

45. Hurtado, J.E.; Alvarez, D.A. Neural-Network-Based Reliability Analysis: A Comparative Study. *Comput. Methods Appl. Mech. Eng.* **2001**, *191*, 113–132. [CrossRef]

46. Naderpour, H.; Kheyroddin, A.; Amiri, G.G. Prediction of FRP-Confined Compressive Strength of Concrete Using Artificial Neural Networks. *Compos. Struct.* **2010**, *92*, 2817–2829. [CrossRef]

47. Dhanya, J.; Raghukanth, S.T.G. Ground Motion Prediction Model Using Artificial Neural Network. *Pure Appl. Geophys.* **2018**, *175*, 1035–1064. [CrossRef]

48. Lagaros, N.D.; Papadrakakis, M.; Fragiadakis, M.; Stefanou, G.; Tsompanakis, Y. Neural Network Aided Stochastic Computations and Earthquake Engineering. *Comput. Assist. Mech. Eng. Sci.* **2007**, *14*, 251–275.

49. Khosravikia, F.; Zeinali, Y.; Nagy, Z.; Clayton, P.; Rathje, E.M. Neural Network-Based Equations for Predicting PGA and PGV in Texas, Oklahoma, and Kansas. *arXiv* **2018**, arXiv:1806.01052.

50. Syifa, M.; Kadavi, P.R.; Lee, C.W. An Artificial Intelligence Application for Post-Earthquake Damage Mapping in Palu, Central Sulawesi, Indonesia. *Sensors* **2019**, *19*, 542. [CrossRef]

51. Tsompanakis, Y.; Lagaros, N.D.; Psarropoulos, P.N.; Georgopoulos, E.C. Simulating the Seismic Response of Embankments via Artificial Neural Networks. *Adv. Eng. Softw.* **2009**, *40*, 640–651. [CrossRef]

52. Arslan, M.H. An Evaluation of Effective Design Parameters on Earthquake Performance of RC Buildings Using Neural Networks. *Eng. Struct.* **2010**, *32*, 1888–1898. [CrossRef]

53. Sakellariou, M.G.; Ferentinou, M.D. A Study of Slope Stability Prediction Using Neural Networks. *Geotech. Geol. Eng.* **2005**, *23*, 419–445. [CrossRef]

54. Pradhan, B.; Lee, S. Landslide Risk Analysis Using Artificial Neural Network Model Focussing on Different Training Sites. *Int. J. Phys. Sci.* **2009**, *4*, 001–015.

55. Pradhan, B.; Lee, S. Regional Landslide Susceptibility Analysis Using Back-Propagation Neural Network Model at Cameron Highland, Malaysia. *Landslides* **2010**, *7*, 13–30. [CrossRef]

56. Mishra, A.K.; Singh, V.P. Drought Modeling—A Review. *J. Hydrol.* **2011**, *403*, 157–175. [CrossRef]

57. Yang, B.; Yin, K.; Lacasse, S.; Liu, Z. Time Series Analysis and Long Short-Term Memory Neural Network to Predict Landslide Displacement. *Landslides* **2019**, *16*, 677–694. [CrossRef]

58. Cho, Y.; Khosravikia, F.; Rathje, E.M. A Comparison of Artificial Neural Network and Classical Regression Models for Earthquake-Induced Slope Displacements. *Soil Dyn. Earthq. Eng.* **2022**, *152*, 107024. [CrossRef]

59. Chakraborty, A.; Goswami, D.D. Slope Stability Prediction Using Artificial Neural Network (ANN). *Int. J. Eng. Comput. Sci.* **2017**, *6*, 21845–21848. [CrossRef]

60. Shokri, M.; Tavakoli, K. A Review on the Artificial Neural Network Approach to Analysis and Prediction of Seismic Damage in Infrastructure. *Int. J. Hydromechatronics* **2019**, *2*, 178–196. [CrossRef]

61. Rachedi, M.; Matallah, M.; Kotronis, P. Seismic Behavior & Risk Assessment of an Existing Bridge Considering Soil-Structure Interaction Using Artificial Neural Networks. *Eng. Struct.* **2021**, *232*, 111800. [CrossRef]

62. Portillo Juan, N.; Negro Valdecantos, V. Review of the Application of Artificial Neural Networks in Ocean Engineering. *Ocean Eng.* **2022**, *259*, 111947. [CrossRef]

63. Liu, Z.; Sextos, A.; Guo, A.; Zhao, W. ANN-Based Rapid Seismic Fragility Analysis for Multi-Span Concrete Bridges. *Structures* **2022**, *41*, 804–817. [CrossRef]

64. Wells, D.L.; Coppersmith, K.J. New Empirical Relationships among Magnitude, Rupture Length, Rupture Width, Rupture Area, and Surface Displacement. *Bull.-Seismol. Soc. Am.* **1994**, *84*, 974–1002.

65. Dassault Systèmes Simulia Abaqus 6.14. *Abaqus 6.14 Anal. User's Guide*; Dassault Systèmes: Shangai, China, 2014.

66. Ni, P.; Moore, I.D.; Take, W.A. Numerical Modeling of Normal Fault-Pipeline Interaction and Comparison with Centrifuge Tests. *Soil Dyn. Earthq. Eng.* **2018**, *105*, 127–138. [CrossRef]

67. Bray, J.D. *The Effects of Tectonic Movements on Stresses and Deformations in Earth Embankments*; University of California: Berkley, CA, USA, 1990.

68. Anastasopoulos, I.; Gazetas, G.; Bransby, M.F.; Davies, M.C.R.; El Nahas, A. Fault Rupture Propagation through Sand: Finite-Element Analysis and Validation through Centrifuge Experiments. *J. Geotech. Geoenvironmental Eng.* **2007**, *133*, 943–958. [CrossRef]

69. Rokonuzzaman, M.; Nahas, A.E.; Sakai, T. Experimental Validation of a Numerical Model for the Interaction of Dip-Slip Normal Fault Ruptures, Sand Deposits, and Raft Foundations. *Int. J. Geotech. Eng.* **2015**, *9*, 239–250. [CrossRef]

70. Thebian, L.; Najjar, S.; Sadek, S.; Mabsout, M. Numerical Investigation of Dip-Slip Fault Propagation Effects on Offshore Seabed Sediments. *Eng. Geol.* **2018**, *237*, 149–167. [CrossRef]

71. Rosso, M.M.; Aloisio, A.; Cucuzza, R.; Pasca, D.P.; Cirrincione, G.; Marano, G.C. Structural Health Monitoring with Artificial Neural Network and Subspace-Based Damage Indicators. In *Proceedings of the Trends on Construction in the Digital Era. ISIC 2022. Lecture Notes in Civil Engineering*; Gomes Correia, A., Azenha, M., Cruz, P.J.S., Novais, P., Pereira, P., Eds.; Springer: Cham, Switzerland, 2022; Volume 306, pp. 524–537.

72. Teslyuk, V.; Kazarian, A.; Kryvinska, N.; Tsmots, I. Optimal Artificial Neural Network Type Selection Method for Usage in Smart House Systems. *Sensors* **2021**, *21*, 47. [CrossRef] [PubMed]

73. Demuth, H.; Beale, M.; Hagan, M. *Neural Network Toolbox 5 User's Guide*; The MathWorks, Inc.: Portola Valley, CA, USA, 2005.

74. Dietterich, T. Overfitting and Undercomputing in Machine Learning. *ACM Comput. Surv.* **1995**, *27*, 251–260. [CrossRef]

75. Lawrence, S.; Giles, C.L.; Tsoi, A.C. Lessons in Neural Network Training: Overfitting May Be Harder than Expected. In *Proceedings of the Fourteenth National Conference on Artificial Intelligence and Ninth Conference on Innovative Applications of Artificial Intelligence, AAAI-97*; AAAI Press: Washington, DC, USA, 1997; pp. 540–545.

76. Jena, R.; Pradhan, B.; Beydoun, G.; Nizamuddin; Ardiansyah; Sofyan, H.; Affan, M. Integrated Model for Earthquake Risk Assessment Using Neural Network and Analytic Hierarchy Process: Aceh Province, Indonesia. *Geosci. Front.* **2020**, *11*, 613–634. [CrossRef]

77. Rosso, M.M.; Marasco, G.; Aiello, S.; Aloisio, A.; Chiaia, B.; Marano, G.C. Convolutional Networks and Transformers for Intelligent Road Tunnel Investigations. *Comput. Struct.* **2023**, *275*, 106918. [CrossRef]

78. Mandal, S.; Prabaharan, N. Ocean Wave Forecasting Using Recurrent Neural Networks. *Ocean Eng.* **2006**, *33*, 1401–1410. [CrossRef]

79. Hagan, M.T.; Menhaj, M.B. Training Feedforward Networks with the Marquardt Algorithm. *IEEE Trans. Neural Netw.* **1994**, *5*, 989–993. [CrossRef]

80. Hagan, M.T.; Demuth, H.B.; Beale, M.H.; De Jesus, O. *Neural Network Design*, 2nd ed.; Martin Hagan: Stillwater, OK, USA, 2014; ISBN 0971732116.

81. Alarifi, A.S.N.; Alarifi, N.S.N.; Al-Humidan, S. Earthquakes Magnitude Predication Using Artificial Neural Network in Northern Red Sea Area. *J. King Saud Univ.-Sci.* **2012**, *24*, 301–313. [CrossRef]

82. Kwag, S.; Hahm, D.; Kim, M.; Eem, S. Development of a Probabilistic Seismic Performance Assessment Model of Slope Using Machine Learning Methods. *Sustainability* **2020**, *12*, 3269. [CrossRef]

83. Ng, C.W.W.; Cai, Q.P.; Hu, P. Centrifuge and Numerical Modeling of Normal Fault-Rupture Propagation in Clay with and without a Preexisting Fracture. *J. Geotech. Geoenvironmental Eng.* **2012**, *138*, 1492–1502. [CrossRef]

84. Ahmadi, M.; Moosavi, M.; Jafari, M.K. Experimental Investigation of Reverse Fault Rupture Propagation through Wet Granular Soil. *Eng. Geol.* **2018**, *239*, 229–240. [CrossRef]

85. Lee, J.W.; Hamada, M. An Experimental Study on Earthquake Fault Rupture Propagation through a Sandy Soil Deposit. *Struct. Eng. Eng.* **2005**, *22*, 1s–13s. [CrossRef]
86. Loukidis, D.; Bouckovalas, G.D.; Papadimitriou, A.G. Analysis of Fault Rupture Propagation through Uniform Soil Cover. *Soil Dyn. Earthq. Eng.* **2009**, *29*, 1389–1404. [CrossRef]
87. Hazeghian, M.; Soroush, A. Numerical Modeling of Dip-Slip Faulting through Granular Soils Using DEM. *Soil Dyn. Earthq. Eng.* **2017**, *97*, 155–171. [CrossRef]
88. Özcebe, A.G.; Paolucci, R.; Mariani, S. Numerical Modeling of the Interaction of Pressurized Large Diameter Gas Buried Pipelines with Normal Fault Ruptures. *Soil Dyn. Earthq. Eng.* **2017**, *101*, 105–115. [CrossRef]